

EFFECTS OF LARGE-AMPLITUDE RF EMISSIONS ON OEDIPUS-C FLOATING VOLTAGES

J.G. Laframboise

Physics and Astronomy Department, York University
4700 Keele Street, Toronto, Canada M3J 1P3.

Phone: 416 736 5621

Fax: 416 736 5516

E-mail: laframboise@quasar.phys.yorku.ca

D.D. Wallis

Magnametrics, Canada

H.G. James

Communications Research Centre, Canada

Abstract

The TCM voltmeter experiment on the OEDIPUS-C tethered payload provided a unique opportunity to compare the charging of two geometrically similar spacecraft, one of which carried a high-voltage RF transmitter. The data from this experiment, together with measurements of ambient plasma parameters from other onboard instruments, have permitted stringent testing of available theories for electron collection by strongly driven antennas in the space plasma. Earlier simple theories have predicted that a transition occurs from rectification-dominated electron collection at low frequencies, causing the spacecraft's floating potential to be driven negative, to ponderomotive-dominated collection at higher frequencies, causing this potential to be driven positive. Our calculation incorporates a model of a transition between these two cases as the frequency increases.

Introduction

The OEDIPUS-C tethered payload (Fig. 1) was launched on 7 November 1995 from the Poker Flat Research Range, Alaska (Fig. 2) [*James and Calvert*, 1998, *James et al.*, 1999, *Prikryl et al.*, 2000, *James*, 2000]. The Tether Current Monitor (TCM) instrument operated the two subpayloads and the conducting tether as a double electrostatic probe. During the part of the experiment discussed here, the flight upleg, the angle between the tether and the geomagnetic-field direction was less than 5 degrees. The TCM configured the payload cyclically as a high-impedance voltage probe and as a low-impedance current probe.

OEDIPUS C also carried a pulsed high-frequency RF exciter (HEX) on its forward subpayload. HEX drove the forward subpayload's V-dipole stems symmetrically with respect to the central point of the RF feed, which was grounded to the spacecraft body.

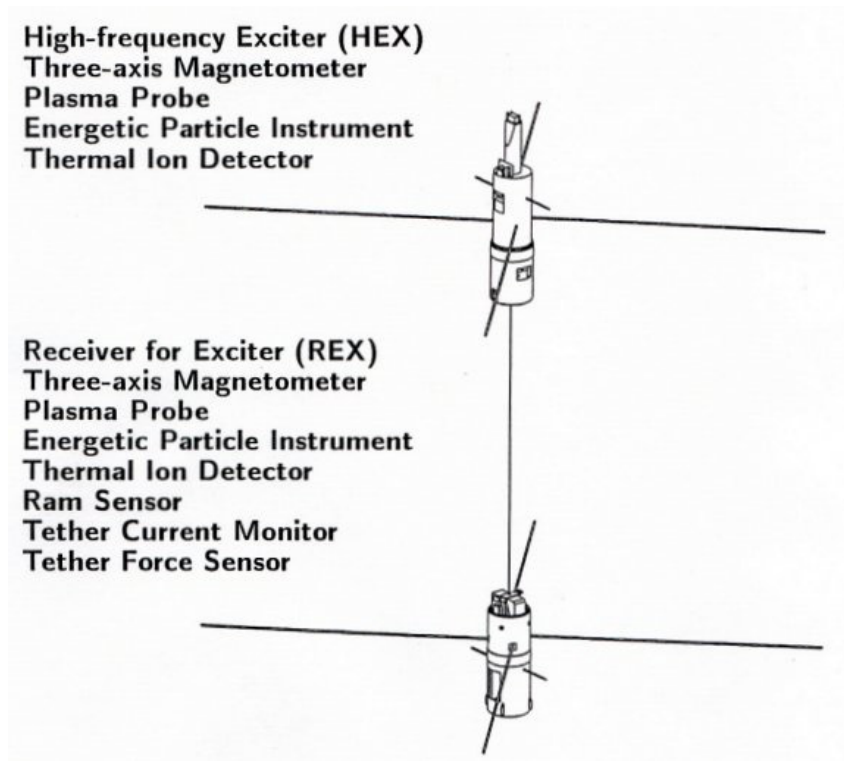


Figure 1. OEDIPUS-C tethered payload, two seconds after separation.

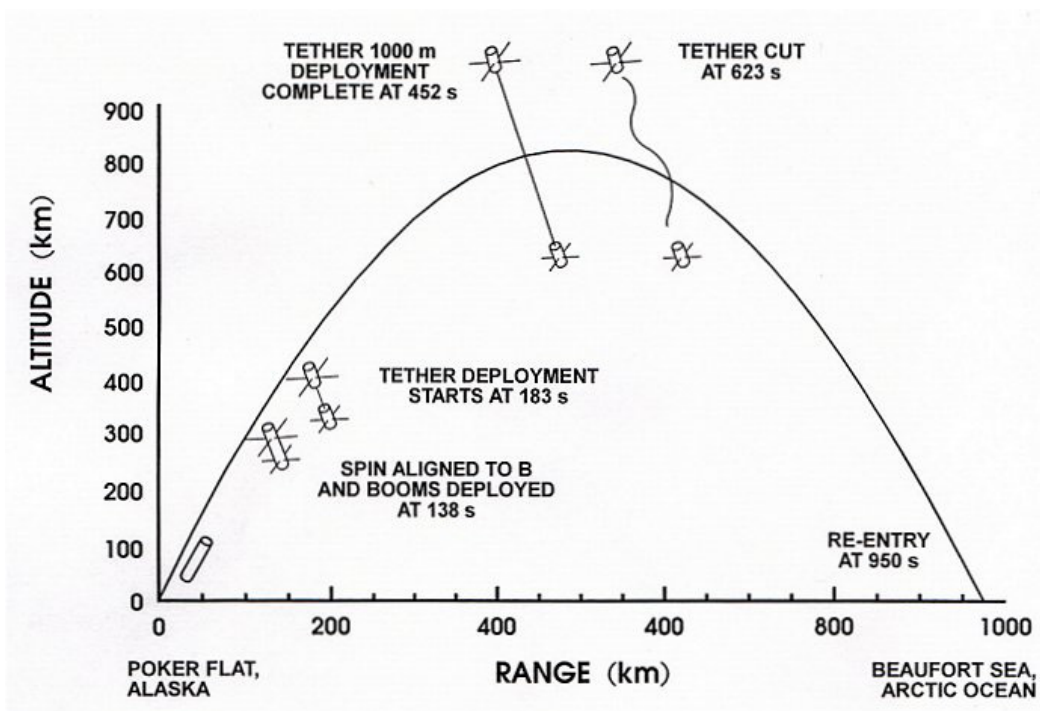


Figure 2. Trajectory of the OEDIPUS-C flight, with major payload events.

The stems of two onboard Langmuir probes were also grounded to the spacecraft body. With the HEX connected to the forward subpayload dipoles and with the frequency of the pulses swept progressively from 25 kHz to 4.1 MHz, the transient response of the TCM voltage showed a number of reproducible features. At the lowest frequencies of the sweep, the RF pulses drove the forward subpayload's potential negative with respect to that of the aft payload (REX) by several tens of volts. The time-constant of relaxation of the payload's potential between the HEX pulses increased as background density decreased.

The TCM voltmeter data (Figs. 3-8) showed a steady rise in the floating voltage of the forward subpayload as the HEX transmitter was swept from lower to higher frequencies. This is as expected when ponderomotive effects become relatively more important relative to rectification. Superposed on this was another feature in which the forward subpayload was driven increasingly negative as the frequency approached the electron gyrofrequency from below, and increasingly positive as it approached it from above. This feature became progressively more evident as background density decreased.

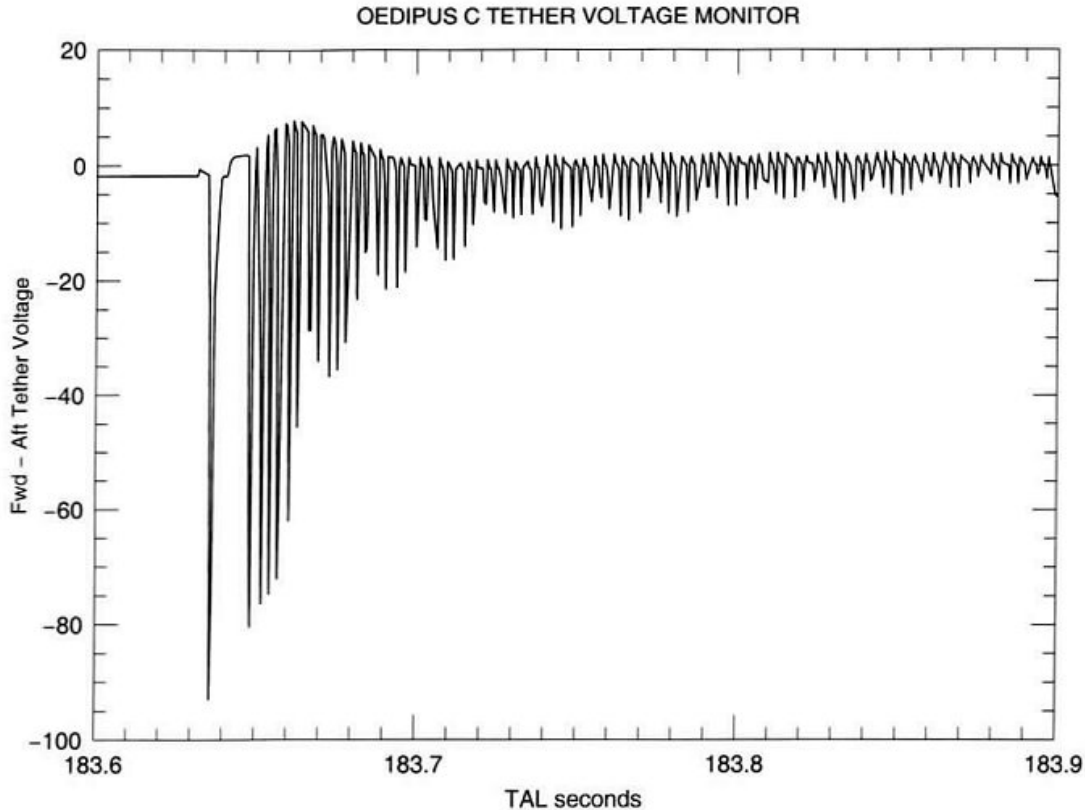


Figure 3. HEX spacecraft voltage relative to that of REX during a frequency sweep by the HEX transmitter. In this and other sweeps shown in subsequent Figures, an initial 600 μ sec pulse at 25 kHz is followed after 12.12 msec by a series of 300 μ sec pulses at intervals of 3.03 msec, having frequencies which begin at 100 kHz and increase by increments of 50 kHz up to 4.1 MHz. During this sweep, measured values of ambient parameters were: $n_e = 4.5 \times 10^3 \text{ cm}^{-3}$, $kT_e/e = 0.34\text{V}$, and induced tether voltage $\mathbf{v} \times \mathbf{B} \cdot \mathbf{L} = 0$, where \mathbf{v} is the spacecraft's velocity and \mathbf{L} is a separation vector directed upward from REX to HEX.

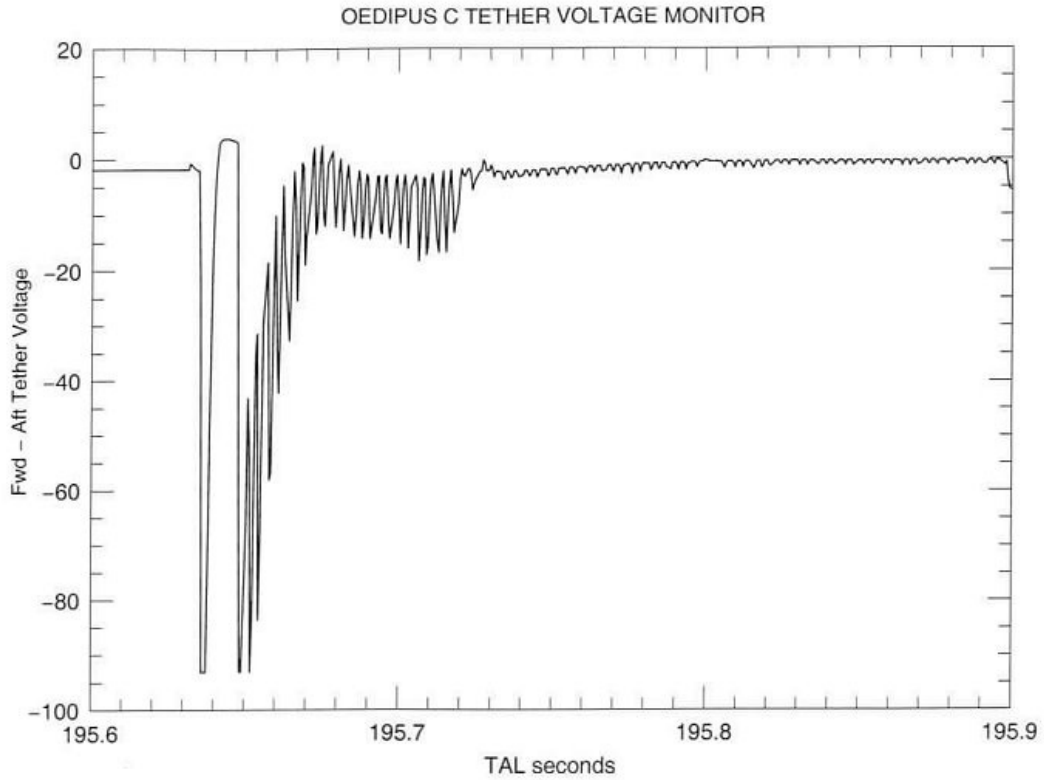


Figure 4. Same as Fig. 3 except that $n_e=6.1 \times 10^3 \text{ cm}^{-3}$, $kT_e/e=0.29\text{V}$, and $v \times B.L=-0.05\text{V}$.

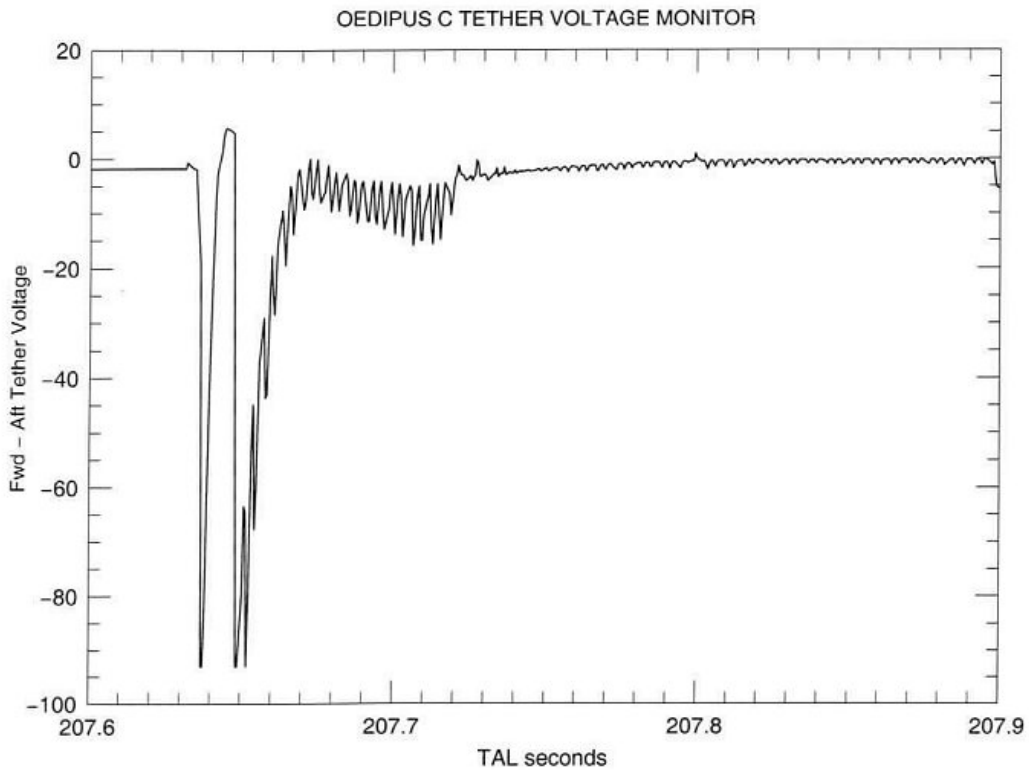


Figure 5. Same as Fig. 3 except that $n_e = 4.1 \times 10^3 \text{ cm}^{-3}$, $kT_e/e = 0.30\text{V}$, and $v \times B.L = -0.09\text{V}$.

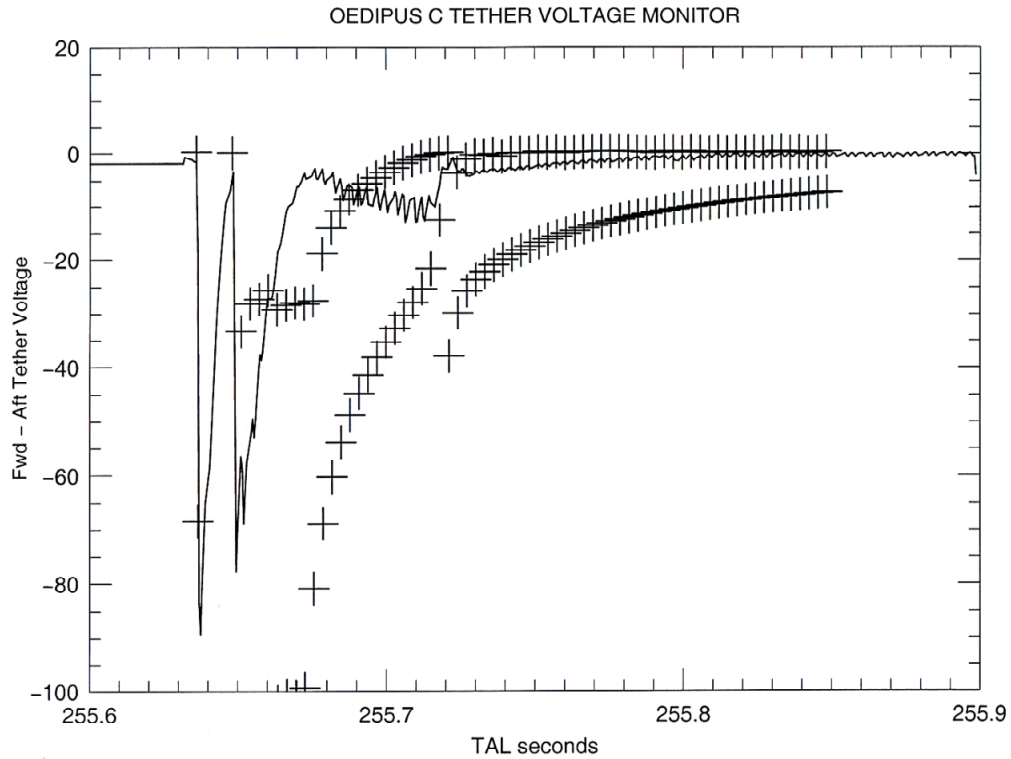


Figure 6. Same as Fig. 3 except that $n_e = 2.5 \times 10^3 \text{ cm}^{-3}$, $kT_e/e = 0.43\text{V}$, and $v \times B.L = -0.27\text{V}$. In Figs. 6-8, preliminary results from our calculation are indicated by crosses, for times corresponding to the beginnings and ends of RF pulses.

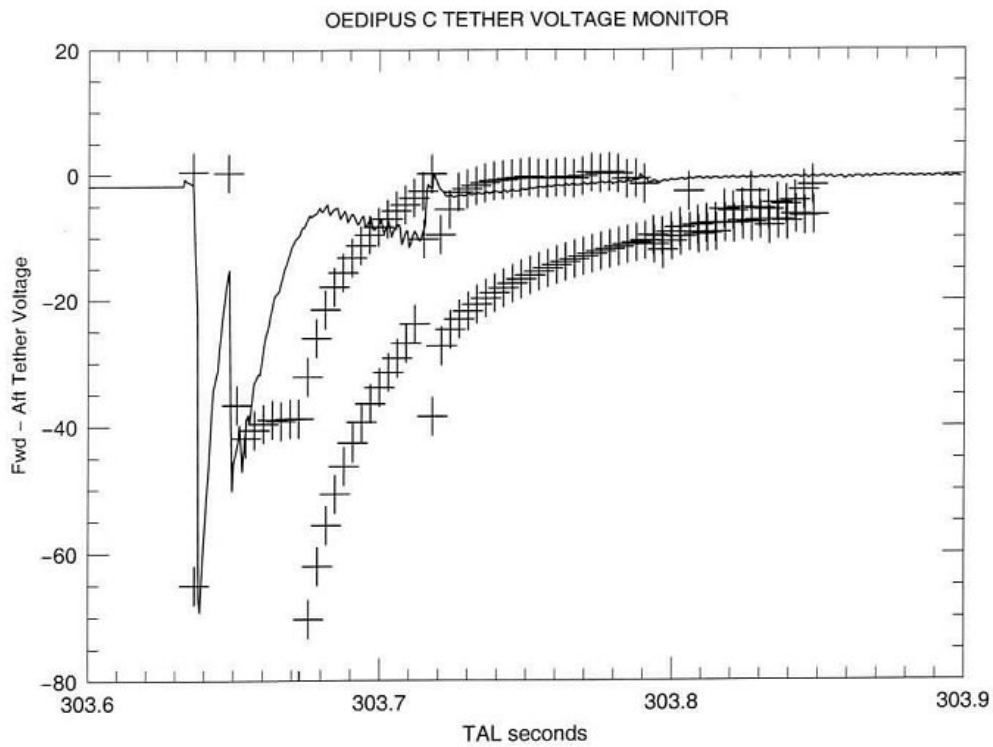


Figure 7. Same as Fig. 3 except that $n_e = 1.5 \times 10^3 \text{ cm}^{-3}$, $kT_e/e = 0.74\text{V}$, and $v \times B.L = -0.45\text{V}$.

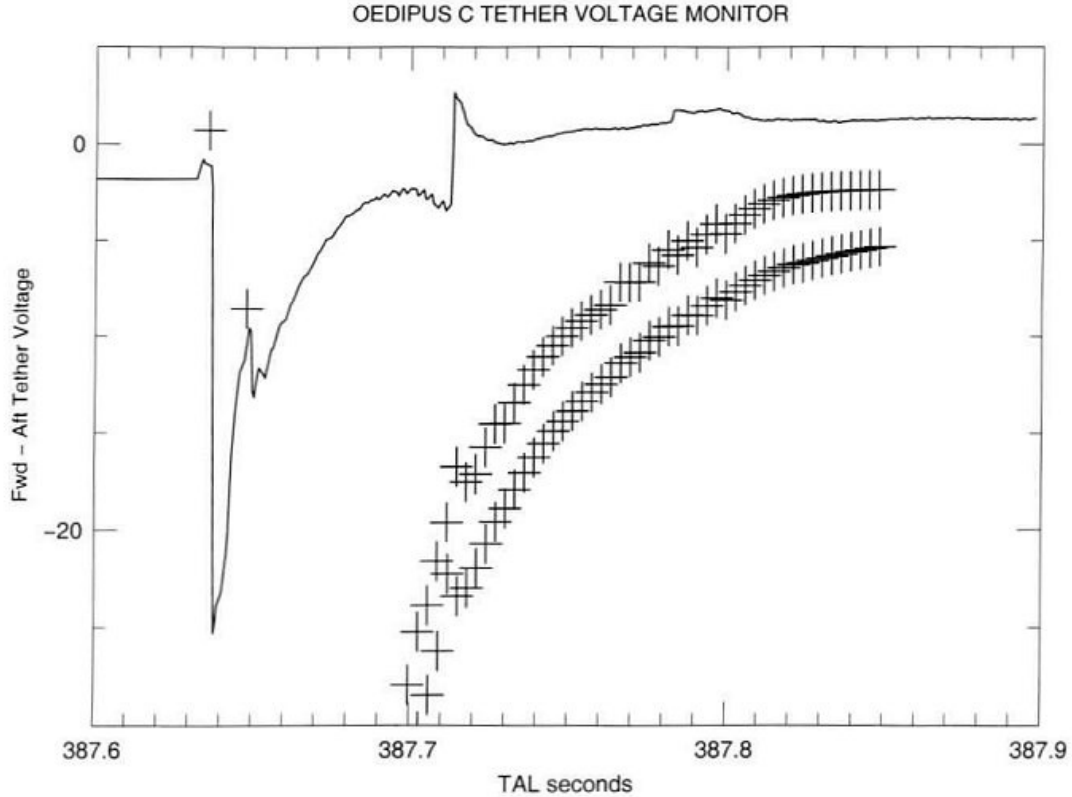


Figure 8. Same as Fig. 3 except that $n_e = 0.3 \times 10^3 \text{ cm}^{-3}$, $kT_e/e = 1.25\text{V}$, and $\mathbf{v} \times \mathbf{B} \cdot \mathbf{L} = -0.68\text{V}$.

It corresponds to a feature which appears in the dependence of the applied RF voltage on frequency, through the dipole impedance theory assumed [Sec. 4, item (2)]. Another feature at twice the electron gyrofrequency also became more evident as background density decreased. Both features are most evident in Fig. 8, at times after launch (TAL) of about 387.713 and 387.783 seconds, respectively.

Also visible in Figs. 3-8 is a succession of positive overshoots in the same voltage following the first few RF pulses in each sweep. As the background density decreases, these overshoots become less evident. In Figs. 4 and 5, the overshoots following the first pulse have had time to reach maximum values and begin to decrease, at times after launch of about 195.645 and 207.645 seconds, respectively. Fitting exponential decay curves to the decreasing voltages following each maximum yields time-constants of approximately 17 and 15 milliseconds. If we assume that these decays are indications of the collapse of an enlarged disturbance-region produced by each RF pulse, and we also assume that this collapse progresses inward at the ion-acoustic-wave speed, then we obtain roughly 46 m and 39 m, respectively, for the characteristic scale of these disturbances. These distances are very large compared with known spatial scales of our situation, including the tip-to-tip length of the HEX V-dipoles (19 m) and the calculated source radius described in Section 3.1.2 (up to about 10 m at the lowest HEX frequencies). We are presently investigating whether these distances correspond to the characteristic scale of the “ponderomotive presheath” which extends beyond this source radius.

In order to investigate these features, we have performed a calculation of the charging and discharging behaviour of HEX relative to that of REX during and between RF pulses as their frequency was swept. Our strategy for these calculations is as follows. We have so far avoided three-dimensional particle-in-cell calculations, because the wide disparities among temporal and spatial scales in the OEDIPUS-C situation appear likely to result in unacceptably long computational times for such calculations. Instead, our approach has been to assume that charging and discharging times are long compared to other time-scales involved, and therefore to use or develop simple parameterizations, for steady-state currents, as functions of spacecraft voltage, collected by all spacecraft surfaces except the HEX dipoles during RF pulses, and for current collection, time-averaged over an RF cycle, by these dipoles during these pulses. Our charging and discharging calculations require us also to use or develop parameterizations for the electric fields, either steady-state or time-averaged over an RF cycle, outside all spacecraft surfaces. Our calculations include effects of time-dependent sheath expansion following the start of RF pulses, and of time-dependent sheath collapse following their end.

Theory

For completeness, we repeat briefly some of the ideas contained in *Rubinstein and Laframboise* [1970] and *Laframboise et al.* [1975]; see also *Laframboise et al.* [2001].

Low frequencies

If the RF field varies slowly enough, the plasma will have time to accommodate itself to the static configuration corresponding to the instantaneous potential of the antenna; “slowly enough” means that the driving frequency ω is small compared with the electron plasma frequency ω_{pe} . Each half of the dipole (each dipole element) then has the static current-voltage characteristic of a Langmuir probe.

With the transmitter off, the antenna is at the Langmuir floating potential, $V_{FL} \sim -kT_e/e$, which is much smaller than the amplitude \tilde{V} of the RF voltage. Here, k is Boltzmann's constant, T_e is the electrons' temperature, and e is the magnitude of unit electronic charge. When the transmitter is switched on, each dipole element becomes positive half the time, with potential up to $+\tilde{V}$, and therefore electron-attracting; the opposite will happen during the next half-cycle, but because the ion saturation current is much smaller than the electron saturation current, the net result will be an increase of negative charge on the element, which will lower its DC potential.

This process will continue until the total (AC + DC) potential of each element is positive and negative during intervals τ_+ and τ_- , respectively, which satisfy:

$$\frac{\tau_-}{\tau_+} \simeq \frac{I_{e,saturation}}{I_{i,saturation}} \quad (1)$$

Under this condition, the net charge gain at the end of a cycle is zero. Since $I_{e,saturation} \gg I_{i,saturation}$, this will happen for

$$V_F \simeq -|\tilde{V}| \ll V_{FL}. \quad (2)$$

High frequencies

In the presence of intense RF emission from a spacecraft antenna, electrons near the antenna are strongly repelled from it due to a nonlinear effect of the emission. This repulsion arises because of the radial oscillations performed by the electrons in the near field of the antenna. At the innermost end-point of such an oscillation (the point nearest the antenna), the outward force due to the near field is stronger than it would be at the same instant at the central point of the oscillation. Conversely, at the outermost end-point, the inwardly directed force is weaker. Therefore, there is a net time-averaged force on the electrons, and to a much smaller extent on ions, directed away from the antenna. It has been shown by a small-amplitude perturbation analysis [*Boot et al.*, 1958] that this time-averaged “ponderomotive” force is equivalent to a static force:

$$-(q^2/4m\omega^2)\nabla(E_1^2) \quad (3)$$

where q and m are the electronic charge and mass, ω is the angular frequency of the RF, and E_1 is the near-field RF electric-field amplitude. The implications of the ponderomotive force for radiating antennas in ionospheric plasmas have been discussed by *Getmantsev and Denisov* [1962], *Whale* [1964], *Rubinstein and Laframboise* [1970, 1972], *Laframboise et al.* [1975], and following Eq. (8) of *Calder et al.* [1993]. Because this force can be expressed as a gradient, its presence is equivalent to the existence of an additional term

$$\phi_a = (q/4m\omega^2)E_1^2 \quad (4)$$

in the static potential as seen by electrons. Therefore it can be incorporated easily into the self-consistent numerical treatment of a cylindrical, perfectly absorbing electrode (Langmuir probe) in a collisionless plasma, already developed for the time-independent case [*Laframboise*, 1966]. Based on this formulation, an analysis of static sheath effects around such an antenna, due to intense RF emission by it, has been published [*Rubinstein and Laframboise*, 1970, *Laframboise et al.*, 1975]. This analysis assumed that E_1 was just the vacuum near-field of the antenna, and hence the approximation $\omega \gg \omega_{pe}$ was implied. For ionospheric sounding antennas of the type carried by the Alouette and ISIS satellites, it predicted enlargement of these antennas' sheaths from a few cm to roughly 1 m radius. This prediction is consistent with ISIS I and II observations [*James*, 1980, Sec. IV].

A more refined analysis has also been published [*Rubinstein and Laframboise*, 1972], in which the restriction to a vacuum near-field was removed by calculating, at each step of the numerical iteration, the dielectric-constant profile implied by the static electron-density profile (the latter having itself been calculated during the previous iteration step), then using this dielectric-constant profile to calculate the modified radial dependence of E_1 for input to the next iteration step. In this manner, the calculation was extended to ω/ω_{pe} ratios down to 1.5. In all of these calculations, the time-averaged force on ions due to the RF was ignored, and we retain this approximation here also.

At cylindrical radii $r \ll$ wavelength λ , and over most of the antenna's length, the instantaneous near field of a cylindrical antenna has the same dependence on position as the static Coulomb field of an infinite cylinder. Hence, we assume that:

$$\mathbf{E}_{rf} = \mathbf{n}_r(c_1/r)\cos \omega t = \mathbf{E}_1 \cos \omega t \quad (5)$$

Substitution into Eq. (4) then yields:

$$\phi_a = (qc_1^2/4m\omega^2)(1/r^2) \quad (6)$$

We introduce a dimensionless additional antenna potential G as follows:

$$G = \frac{q\phi_{aA}}{kT} = \frac{q^2 c_1^2}{4m\omega^2 r_A^2 kT} \quad (7)$$

where ϕ_{aA} and r_A represent additional potential and radius at the antenna's surface, and $q = -e$. The input parameters for static sheath calculations are then three in number: the value of G , the value of the dimensionless antenna static potential $\psi_A = e\phi_A/kT$, and the antenna Debye ratio $r_A/\lambda_D = r_A/(e^2 n_\infty/\epsilon_0 kT)^{1/2}$. Here, n_∞ is the electron or ion number density far from the antenna, and ϵ_0 is the permittivity of free space. We have eliminated the ion-to-electron temperature ratio T_i/T_e as a parameter by assuming that $T_i = T_e \equiv T$ throughout.

Intermediate frequencies

The preceding discussion implies that at low frequencies, we expect the rectification effect to predominate, and the spacecraft to be driven negative. Conversely, at high frequencies, we expect the ponderomotive effect to predominate, and the spacecraft to be driven positive. A central issue in modeling the TCM voltmeter results then is: how do we describe the transition from one to the other? We address this issue in Section 3.1.2.

Ion and Electron Collection by Spacecraft Surfaces

These surfaces include the HEX and REX spacecraft bodies, dipoles, and probe stems. We assume that collisionless theory applies throughout.

Electron collection

We ignore the spacecraft's speed compared with the electron (but not the ion) thermal speed. We ignore all end-effects and effects of interactions among spacecraft bodies, dipoles, and probe stems.

HEX and REX spacecraft bodies:

We ignore the misalignment of these bodies with the geomagnetic field \mathbf{B} ; this was less than 5° during the analyzed portion of the flight. For electron-attracting (positive) surface potentials, measured relative to space potential, we use the lesser of the canonical-upper-bound current prediction for a finite cylindrical probe aligned with \mathbf{B} [*Rubinstein and Laframboise*, 1982, Eqs. (30), (33)-(35), and 1983, Sec. 2B], and the *Mott-Smith and Langmuir* [1926] orbital-motion-limited current prediction for a spherical probe; reasons for this choice are discussed in *Laframboise and Parker* [1973]. For electron-repelling (negative) surface potentials, we use the

lesser of the current given by *Rubinstein and Laframboise* [1982, Eqs. (30), (36), and (37)], and the Boltzmann factor.

HEX radiating dipoles:

We obtain sheath and presheath potential distributions using a two-region approximation of the theory of *Laframboise et al.* [1975, Figures 3-8]. In this approximation, the sheath region is assumed to contain a uniform density of ions only, and the presheath region is assumed quasineutral, with ponderomotive repulsion of electrons only. The potential and the electric field are assumed to be continuous at the sheath-edge. We calculate a “source radius” for electrons collected on the dipole elements, by using the lesser of: (a) the steady-state sheath-edge radius given by the two-region approximation, or (b) an expanding sheath-edge radius which is assumed to move outward at the ion-acoustic-wave speed, starting at the antenna radius r_A at the beginning of each RF pulse. The use of this expanding radius is suggested by the expanding ion-acoustic wavefronts seen in Fig. 13 of *Calder et al.* [1993]. We also assume that the alternating electric field is given by Eq. (5) between r_A and this source radius, and that the electron distribution at this source radius is a steady-state Maxwellian which includes a Boltzmann factor based on the combined electrostatic and ponderomotive potentials at this radius. These assumptions provide an electron-collection model which incorporates both the rectification effect described in Section 2.1 and the ponderomotive effect described in Section 2.2.

Probe stems, HEX dipoles between RF pulses, and REX nonradiating dipoles:

For positive surface potentials, we use the lesser of the canonical-upper-bound current prediction for infinite-cylindrical probes inclined to \mathbf{B} [*Rubinstein and Laframboise*, 1978, Eq. (11)], and the orbital-motion-limited current prediction for infinite-cylindrical probes [*Mott-Smith and Langmuir*, 1926, Eq. (29)]. For negative surface potentials, we use the lesser of the currents given by the corresponding canonical-upper-bound prediction for repelling probes [*Rubinstein and Laframboise*, 1978, Eq. (13)], and the Boltzmann factor.

Ion collection

HEX and REX spacecraft bodies, REX nonradiating dipoles, and probe stems:

The ions' average gyroradius is much larger than the spacecraft dimensions, so magnetic-field effects on ion collection can be neglected. However, the spacecraft speed is comparable to the ion thermal speed, and therefore ion drift effects cannot be neglected. Available theory for this situation [*Godard and Laframboise*, 1983], combines ion drift with available self-consistent potentials for corresponding *nondrifting* cases. However, the results of this theory are in tabular form, which is inconvenient for our purposes, and may not cover the complete range of external parameters found in our situation.

Therefore, we approximate further as follows. Around each of the spacecraft bodies, dipole elements, and probe stems, we separately assume cylindrical symmetry of the sheath potential distribution. For negative (ion-attracting) surface potentials, we calculate the sheath potential distribution using a uniform-ion-density, zero-electron-density model. We then approximate the

more realistic drifting Maxwellian ion distribution by a monokinetic one whose total kinetic energy includes transverse drift and thermal energies. Specifically, if U_n is the component of ion drift speed transverse to the cylinder's axis, we assume that every ion has transverse kinetic energy $\frac{1}{2} m_i U_n^2 + \frac{1}{4} \pi kT$ far from the cylinder's surface; this choice gives the correct current for zero drift and zero surface-potential [*Laframboise*, 1966, Eq. (10.11)]. We assume that ion collection is limited by the least angular momentum of accelerated ions which can exist at any radius from the collector to the sheath-edge. The result is a simple numerical approximation for ion collection. For sufficiently positive (ion-repelling) surface potentials $q\phi_s > \frac{1}{2} m_i U_n^2$, we approximate the ion collection very crudely by a modified Boltzmann factor $\exp[(-q\phi_s + \frac{1}{2} m_i U_n^2) / kT_i]$ times the random ion current.

HEX radiating dipoles

For these, we use an ion-collection model similar to that described just above, but modified to include the ion-repelling potential peak predicted by the two-region model potential described earlier [Section 3.1.2 above].

Further Details of the Calculation

- (1) Effects of finite HEX driving frequency (compared to the electron plasma frequency) on the ponderomotive presheath potential distribution are included. This permits our calculation to extend over the full range of HEX driving frequencies, both below and above ω_{pe} .
- (2) Driving voltages across the HEX V-dipole terminals are used directly to provide electric-field amplitudes as functions of radius. The voltages are computed using an equivalent-circuit analysis of the HEX power amplifier and dipoles [James, 2003].
- (3) The HEX dipole elements' finite lengths (9.28m) cause the ponderomotive repulsion to decrease more steeply at radii comparable to these lengths. We have included this effect, by approximating the alternating electric-field distribution outside each dipole element by that outside a prolate spheroid having the same length-to-diameter ratio.
- (4) We have rederived the ponderomotive repulsion including the geomagnetic field B. Our results indicate that electrons are repelled only along B, not across B. Therefore the curvature of the alternating electric field E away from B diminishes this repulsion, especially near the dipole elements' roots where this curvature is largest. This situation suggests that electron collection at lowest frequencies may occur mostly near these roots. We have included this effect by approximating the electric-field lines connecting opposite dipole elements very crudely as semicircles centered on the central point of the antenna.

Acknowledgments

We are grateful to K.G. Balmain for valuable discussions and comments. One of us (J.G.L.) was supported by the Natural Sciences and Engineering Research Council of Canada under grant A-4638.

References

1. Boot, H.A.H., S.A. Self, and R.B.R. Shersby-Harvie, Containment of a fully-ionized plasma by radio-frequency fields, *J. Electron. Control*, 4(5), 434, 1958.
2. Calder, A.C., G.W. Hulbert, and J.G. Laframboise, Sheath dynamics of electrodes stepped to large negative potentials, *Phys. Fluids B*, 5(3), 674, 1993.
3. Getmantsev, C.G., and N.G. Denisov, Concerning an effect during measurement of electron concentration in the ionosphere by the antenna probe method, *Geomagn. Aeronomy*, 2, 575, 1962.
4. Godard, R., and J.G. Laframboise, Total current to cylindrical collectors in collisionless plasma flow, *Planet. Space Sci.* 31(3), 275, 1983.
5. James, H. Gordon, Tests of impedance theories for a transmitting dipole in an ionospheric plasma, *IEEE Trans. Antennas Propagation*, AP-28(5), 623, 1980.
6. James, H.G., Ionospheric duct parameters from a dual-payload radio-frequency sounder, *J. Geophys. Res.*, 105(A9), 20,909, 2000.
7. James, H.G., Electromagnetic whistler-mode radiation from a dipole in the ionosphere, *Radio Science* 38(1), 1009, doi: 10.1029/2002RS 002609, 2003.
8. James, H.G., and W. Calvert, Interference fringes detected by OEDIPUS C, *Radio Science*, 33(3), 617, 1998.
9. James, H.G., V.I. Sotnikov, W.J. Burke, and C.Y. Huang, OEDIPUS-C observations of electrons accelerated by radio frequency fields at whistler-mode frequencies, *Phys. Plasmas*, 6(10), 4058, 1999.
10. Laframboise, J.G., Theory of spherical and cylindrical Langmuir probes in a collisionless, Maxwellian plasma at rest, Rep. 100, Institute for Aerospace Studies, University of Toronto, Toronto, Ontario, Canada, 1966.
11. Laframboise, J.G., and L.W. Parker, Probe design for orbit-limited current collection, *Phys. Fluids*, 16(5), 629, 1973.
12. Laframboise, J.G., J. Rubinstein, and F.H. Palmer, Theory of topside sounder transmission effects on antenna quasistatic sheath impedance, *Radio Science*, 10(8,9), 773, 1975.

13. Laframboise, J.G., D.D. Wallis, and H.G. James, RF effects on OEDIPUS-C floating voltages, in: Proceedings of the 7th Spacecraft Charging Technology Conference, edited by R.A. Harris, 23-27 April 2001, ESTEC, Noordwijk, The Netherlands, ESA SP-476, November 2001, pp. 309-314.
14. Mott-Smith, H.M., and I. Langmuir, The theory of collectors in gaseous discharges, *Phys. Rev.*, 28(4), 727, 1926.
15. Prikryl, P., H.G. James, D.J. Knudsen, S.C. Franchuk, H.C. Stenbaek-Nielson, and D.D. Wallis, OEDIPUS-C topside sounding of a structured auroral E region, *J. Geophys. Res.* 105(A1), 193, 2000.
16. Rubinstein, J., and J.G. Laframboise, Plasma sheath around a floating cylindrical antenna at high power, *Can. J. Phys.*, 48(16), 1882, 1970.
17. Rubinstein, J., and J.G. Laframboise, Ion temperature diagnostic using a high power alternating current probe, *Phys. Fluids*, 15(7), 1259, 1972.
18. Rubinstein, J., and J.G. Laframboise, Upper-bound current to a cylindrical probe in a collisionless magnetoplasma, *Phys. Fluids*, 21(9), 1655, 1978.
19. Rubinstein, J., and J.G. Laframboise, Theory of a spherical probe in a collisionless magnetoplasma, *Phys. Fluids*, 25(7), 1174, 1982.
20. Rubinstein, J., and J.G. Laframboise, Theory of axially symmetric probes in a collisionless magnetoplasma: aligned spheroids, finite cylinders, and disks, *Phys. Fluids*, 26(12), 3624, 1983.
21. Whale, H.A., Ion sheath effects near antennas radiating within the ionosphere, *J. Geophys. Res.*, 69(3), 447, 1964.